Programmable topotaxis of magnetic rollers in time-varying fields

Journal:	*Soft Matter*
Manuscript ID	SM-ART-08-2020-001443.R1
Article Type:	Paper
Date Submitted by the Author:	09-Nov-2020
Complete List of Authors:	Dou, Yong; Columbia University, Chemical Engineering Tzelios, Peter; Columbia University, Chemical Engineering Livitz, Dimitri; Columbia University, Chemical Engineering Bishop, Kyle; Columbia University, Chemical Engineering; Columbia University

Soft Matter

ARTICLE TYPE

Cite this: DOI: 00.0000/xxxxxxxxxx

Received Date
Accepted Date

DOI: 00.0000/xxxxxxxxxx

Programmable topotaxis of magnetic rollers in time-varying fields†

Yong Dou,[a] Peter M. Tzelios[a], Dimitri Livitz[a] and Kyle J. M. Bishop*[a]

We describe how spatially uniform, time-periodic magnetic fields can be designed to power and direct the migration of ferromagnetic spheres up (or down) local gradients in the topography of a solid substrate. Our results are based on a dynamical model that considers the time-varying magnetic torques on the particle and its motion through the fluid at low Reynolds number. We use both analytical theory and numerical simulation to design magnetic fields that maximize the migration velocity up (or down) an inclined plane. We show how "topotaxis" of spherical particles relies on differences in the hydrodynamic resistance to rotation about axes parallel and perpendicular to the plane. Importantly, the designed fields can drive multiple independent particles to move simultaneously in different directions as determined by gradients in their respective environments. Experiments on ferromagnetic spheres provide evidence for topotactic motions up inclined substrates. The ability to program the autonomous navigation of driven particles within anisotropic environments is relevant to the design of colloidal robots.

1 Introduction

The autonomous navigation of active or driven particles within anisotropic environments is an essential capability in creating colloidal robots[1,2] that operate without external supervision and control. Inspired by chemotactic bacteria that swim up (or down) gradients in the concentration of a chemoattractant (or repellant), active colloids can now direct their self-propelled motions in response to gradients in chemical concentrations,[3] magnetic potential,[4] light intensity,[5,6] fluid velocity,[7,8] fluid viscosity,[9] and gravitational potential.[10,11] Typically, these navigation strategies rely on gradient-driven torques to rotate anisotropic particles in a preferred orientation, thereby directing their motion—often by a different mechanism. For example, Janus spheres orient their denser hemisphere downward in a gravitational field to direct their self-phoretic propulsion upward against the gravity direction.[10] Owing to their dependence on gradient-driven torques, these strategies are less effective in weak gradients where other torques—for example, due to Brownian motion or self-propulsion—have a stronger influence on particle orientation.

Recently, we proposed a strategy to navigate weak gradients by using stimuli-responsive colloids[12] as high-gain sensors to inform the shape-directed motions of shape-shifting particles.[13] By carefully selecting the shape of the particle and its stimulus response, one can program autonomous motions in different directions relative to the gradient. More generally, particle shape[14,15] and composition[16] provide a rich design space with which to encode the desired behaviors of active colloids. However, the realization of these designs can present challenges in synthesizing complex anisotropic particles.

Alternatively, time-varying magnetic fields in three-dimensions (3D) provide an experimentally accessible design space, with which to direct complex motions of even simple particles. Rotating fields induce torques on magnetic particles,[17] which drive their rotation and translation near solid substrates due to hydrodynamic interactions.[18] In this way, ferromagnetic spheres with residual magnetic moments[19] as well as superparamagnetic particles with anisotropic susceptibilities[20] are driven to "roll" on planar substrates as directed by the external field. Recent work on these colloidal rollers has focused on their collective be-

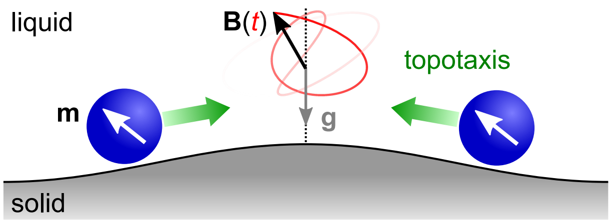

Fig. 1 Topotaxis of ferromagnetic rollers. Spherical particles with permanent magnetic moments $\mathbf{m}$ are immersed in a viscous liquid above a solid substrate with long-wave topographies. Spatially uniform, time-periodic magnetic fields $\mathbf{B}(t)$ are designed to drive particle migration up the local topographic gradients.

---

[a] Department of Chemical Engineering, Columbia University, New York, NY, USA
* kyle.bishop@columbia.edu

† Electronic Supplementary Information (ESI) available: resistance parameters κ and λ as a function of surface separation δ; dimensionality reduction by PCA; effects of gravity. See DOI: 10.1039/cXsm00000x/

haviors within dynamic assemblies such as crystals,[21] flocks,[22] swarms,[23,24] worms,[25] wheels,[26] and critters.[19] At the level of individual particles, there remain interesting questions on the influence of particle shape[27] and surface topography[28] on propulsion dynamics in simple time-periodic fields (e.g., oscillating, rotating, precessing).

Here, we investigate the use of more complex time-varying fields to inform the dynamics of ferromagnetic spheres moving in a viscous fluid above an inclined plane (Fig. 1). We show how designed fields can be used to encode steady particle motions up (or down) the inclined surface *without* knowledge of its orientation or the particle's location. Importantly, the applied field does not instruct the particle on which direction to move but rather on how to respond to local variations in the particle environment. As a result, the same field can drive multiple independent particles to move simultaneously in different directions as determined by local gradients in the surface topography. We refer to these gradient-driven motions as *topotaxis* by analogy to the biological phenomenon of the same name.[29]

Our results are based on a dynamical model that considers the time-varying magnetic torques on the particle and its resulting motion through the fluid at low Reynolds number. Using a two-timing perturbation scheme, we develop analytical approximations for the drift velocity accurate to first order in the incline angle and to second order in the driving frequency. This analysis reveals that topotactic motions rely on differences in the hydrodynamic resistance to rotation about axes parallel and perpendicular to the plane. Using numerical simulations, we identify complex driving fields that maximize the speed of gradient-driven motion up (or down) the inclined surface. Experiments on ferromagnetic spheres subject to these time varying fields provide evidence for particle topotaxis up inclined substrates. Together, our results demonstrate how complex time-varying fields can be used to both power and instruct the autonomous behavior of colloidal particles in anisotropic environments.

2 Ferromagnetic Rollers

We consider a magnetic sphere with radius a and permanent magnetic moment $\mathbf{m}$ moving through a viscous fluid at a fixed height above a solid plane under the influence of a time-varying magnetic field $\mathbf{B}(t)$. In a uniform field, the particle experiences a magnetic torque, $\mathbf{L} = \mathbf{m} \times \mathbf{B}(t)$, but no magnetic force, $\mathbf{F} = 0$. In the absence of inertial effects (i.e., at low Reynolds number), the magnetic force and torque on the particle are balanced by the hydrodynamic force and torque, which are related to the particle's linear velocity $\mathbf{U}$ and angular velocity $\boldsymbol{\Omega}$ as

$$\begin{bmatrix} \mathbf{F} \\ \mathbf{L} \end{bmatrix} = \begin{bmatrix} A & \tilde{B} \\ B & C \end{bmatrix} \begin{bmatrix} \mathbf{U} \\ \boldsymbol{\Omega} \end{bmatrix} \tag{1}$$

where A, B, $\tilde{B}$, and C are components of the hydrodynamic resistance matrix.

For a solid sphere above a solid plane normal to the z-direction, the components of the resistance tensor have the form

$$A = 6\pi\eta a \begin{bmatrix} Y_A & \cdot & \cdot \\ \cdot & Y_A & \cdot \\ \cdot & \cdot & X_A \end{bmatrix} \tag{2}$$

$$B = -\tilde{B} = 6\pi\eta a^2 \begin{bmatrix} \cdot & Y_B & \cdot \\ -Y_B & \cdot & \cdot \\ \cdot & \cdot & \cdot \end{bmatrix} \tag{3}$$

$$C = 6\pi\eta a^3 \begin{bmatrix} Y_C & \cdot & \cdot \\ \cdot & Y_C & \cdot \\ \cdot & \cdot & X_C \end{bmatrix} \tag{4}$$

where η is the fluid viscosity. The coefficients Y_A and Y_B describe, respectively, the dimensionless force and torque on a sphere translating parallel to a solid planar surface.[30] The coefficient Y_C describes the torque on a sphere rotating about an axis parallel to the surface.[31] The coefficient X_A describes the force on a sphere translating perpendicular to the surface.[32] Finally, X_C describes the torque on a sphere rotating about an axis perpendicular to the surface.[33] These coefficients depend only on the surface separation, $\delta = z_p - a$, scaled by the particle radius a.

Substituting the above expressions for the resistance tensor, the linear and angular velocity can be expressed explicitly in terms of the magnetic torque as

$$6\pi\eta a^2 \mathbf{U} = \frac{Y_A}{Y_A Y_C - Y_B^2} \begin{bmatrix} \cdot & \kappa & \cdot \\ -\kappa & \cdot & \cdot \\ \cdot & \cdot & \cdot \end{bmatrix} \mathbf{L} \tag{5}$$

$$6\pi\eta a^3 \boldsymbol{\Omega} = \frac{Y_A}{Y_A Y_C - Y_B^2} \begin{bmatrix} 1 & \cdot & \cdot \\ \cdot & 1 & \cdot \\ \cdot & \cdot & \lambda \end{bmatrix} \mathbf{L} \tag{6}$$

where $\kappa = Y_B / Y_A$ and $\lambda = (Y_A Y_C - Y_B^2)/(Y_A X_C)$. These dynamics imply that the particle velocity normal to the planar substrate is identically zero (i.e., $U_z = 0$). We therefore assume that the surface separation δ and the resistance coefficients are constant throughout the particle's dynamics. For a surface separation of $\delta = 0.01a$, the dimensionless parameters are $\kappa = 0.108$ and $\lambda = 1.87$ (see Supporting Figure S1 for plots of κ and λ vs. δ/a).

Our present analysis neglects the effects of gravity and of Brownian motion. A gravitational force normal to the surface is implicit in our assumption of a constant surface separation δ. Gravity-driven motions tangent to the surface are assumed to be negligible compared to those induced by the magnetic field. As detailed below, this assumption is valid when $F_g a / m B_0 \ll 0.01$, where F_g is the gravitational force on the particle. Similarly, we assume that magnetic torques are sufficiently large as to neglect Brownian motion, which is appropriate when $k_B T / m B_0 \ll 1$ where $k_B T$ is the thermal energy.

2.1 Non-dimensionalization

To facilitate both numerical solution and analytical analysis of the particle dynamics, it is convenient to introduce dimensionless variables using the following scales

$$\begin{aligned} &\text{field: } B_0 \\ &\text{torque: } mB_0 \\ &\text{length: } a \\ &\text{time: } \omega_0^{-1} \equiv \frac{6\pi\eta a^3 (Y_A Y_C - Y_B^2)}{mB_0 Y_A} \end{aligned} \tag{7}$$

Here, B_0 is the characteristic magnitude of the applied field, and ω_0 is the particle relaxation rate. In dimensionless form, the dynamical equations (5) and (6) depend on the two constant parameters κ and λ along with the time-varying magnetic field $\mathbf{B}(t)$. Below, we use the same notation to refer to dimensionless quantities, which corresponds to setting the characteristic scales to unity in the dynamical equations (5) and (6) (e.g., $a \to 1$).

2.2 Euler Angle Dynamics

The dynamics of equations (5) and (6) are solved numerically to determine the particle position $\mathbf{x}_{\mathrm{p}}(t)$ and its orientation parameterized by the Euler angles $\mathbf{u} = [\phi, \theta, \psi]^T$. At each point in time, the magnetic torque $\mathbf{L}$ expressed in the surface coordinate system (Fig. 2) is given by

$$\mathbf{L} = (R_{313}^T(\mathbf{u})\ \mathbf{m}'') \times \mathbf{B}(t) \tag{8}$$

where $\mathbf{m}'' = [0,0,1]^T$ is the constant magnetic moment expressed in the particle coordinate system, and $R_{313}(\mathbf{u}) = R_3(\phi)R_1(\theta)R_3(\psi)$ is the rotation matrix for the $(3,1,3)$ sequence of Euler angles.[34] Given the torque $\mathbf{L}$, the linear velocity $\mathbf{U}$ and angular velocity $\boldsymbol{\Omega}$ are given by equations (5) and (6), respectively. Starting from initial conditions $\mathbf{x}_p(0)$ and $\mathbf{u}(0)$, the position and orientation evolve as

$$\dot{\mathbf{x}}_p = \mathbf{U} \tag{9}$$

$$\dot{\mathbf{u}} = \frac{1}{s_\theta} \begin{bmatrix} s_\psi & -c_\psi & 0 \\ s_\theta c_\psi & s_\theta s_\psi & 0 \\ -s_\psi c_\theta & c_\psi c_\theta & s_\theta \end{bmatrix} \cdot \boldsymbol{\Omega} \tag{10}$$

with $c_x = \cos(x)$ and $s_x = \sin(x)$.[34] The resulting dynamical equations for the particle orientation can be simplified as

$$\dot{\phi} = -\cot\theta(B_x \cos\psi + B_y \sin\psi) \tag{11}$$

$$\dot{\theta} = -\cos\theta(B_y \cos\psi - B_x \sin\psi) - B_z \sin\theta \tag{12}$$

$$\dot{\psi} = \tfrac{1}{2}\left((1+\lambda) + (1-\lambda)\cos 2\theta\right)\csc\theta(B_x \cos\psi + B_y \sin\psi) \tag{13}$$

Note that the dynamics of the angles θ and ψ can be solved independently of ϕ. This simplification follows from the fact that there is no torque on the particle about the axis of its magnetic moment. Similarly, the particle velocity in the plane of the substrate can be expressed as

$$U_x = \kappa(B_x \cos\theta - B_z \sin\psi \sin\theta) \tag{14}$$

$$U_y = \kappa(B_y \cos\theta + B_z \cos\psi \sin\theta) \tag{15}$$

Equations (12)–(15) can be integrated numerically to determine the motion of the particle in the prescribed magnetic field $\mathbf{B}(t)$.

2.3 Two-Timing Perturbation Solution

For time-periodic magnetic fields of frequency ω, the particle dynamics can be approximated using a perturbation expansion based on *two-timing*,[35] where the dimensionless frequency is treated as the small parameter. Physically, this parameter represents the ratio between the driving frequency of the applied field and the relaxation rate of the magnetic particle. The assumption that $\omega \ll 1$ implies that relaxation is fast, such that the particle's magnetic moment aligns closely with the field. Under these conditions, we can introduce two time variables: a slow time, $T = \omega t$, corresponding to the driving field and a fast time, $\tau = t$, corresponding to particle relaxation. The solution to equations (12)–(15) can then be expanded as

$$\theta(t,\omega) = \theta_0(\tau,T) + \omega\theta_1(\tau,T) + \omega^2\theta_2(\tau,T) + O(\omega^3) \tag{16}$$

$$\psi(t,\omega) = \psi_0(\tau,T) + \omega\psi_1(\tau,T) + \omega^2\psi_2(\tau,T) + O(\omega^3) \tag{17}$$

$$\mathbf{U}(t,\omega) = \omega\mathbf{U}_1(\tau,T) + \omega^2\mathbf{U}_2(\tau,T) + O(\omega^3) \tag{18}$$

where τ and T and treated as independent variables. Substituting these expansions into the governing equations and collecting like powers in ω, we obtain a hierarchy of perturbation equations that can be solved sequentially. We are primarily interested in the slow time dynamics of the particle over one cycle of the oscillation period; we therefore focus on the limit as $\tau \to \infty$ in which the fast processes have fully relaxed.

At the periodic steady-state ($\tau \to \infty$), the average velocity $\langle \mathbf{U} \rangle$

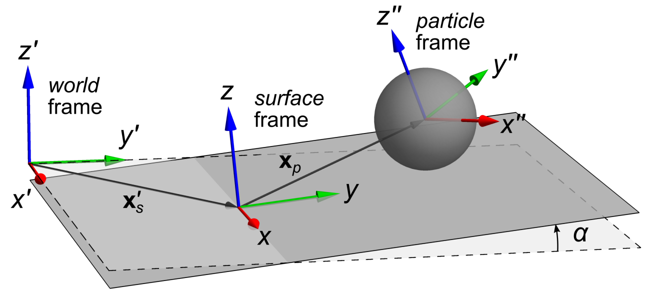

Fig. 2 Three coordinate systems used to describe particle motion.[34] A point $\mathbf{x}$ in the *surface* coordinates is related to the same point $\mathbf{x}'$ in the *world* coordinates as $\mathbf{x} = R_1(\alpha)(\mathbf{x}' - \mathbf{x}'_s)$. Here, the matrix $R_1(\alpha)$ denotes rotation about the x-axis by an angle α; the vector $\mathbf{x}'_s$ is the origin of the surface coordinates expressed in the world coordinates. Similarly, a point $\mathbf{x}''$ in the *particle* coordinates is related to the same point $\mathbf{x}$ in the *surface* coordinates as $\mathbf{x}'' = R_{313}(\mathbf{u})(\mathbf{x} - \mathbf{x}_p)$ where $R_{313}(\mathbf{u}) = R_3(\phi)R_1(\theta)R_3(\psi)$ is the rotation matrix for the (3,1,3) sequence of Euler angles $\mathbf{u} = [\phi, \theta, \psi]^T$.

of the particle is given by the following integral of the slow time over one oscillation cycle

$$\langle \mathbf{U} \rangle = \frac{1}{2\pi} \int_0^{2\pi} \mathbf{U}(\infty, T) dT \tag{19}$$

where the components of the velocity are given by equations (14) and (15). Substituting the perturbation expansion (18), the average velocity can be expanded as

$$\langle \mathbf{U} \rangle = \omega \langle \mathbf{U}_1 \rangle + \omega^2 \langle \mathbf{U}_2 \rangle + O(\omega^3) \tag{20}$$

Note that the zeroth order contributions are identically zero as there is no motion in the limit of zero frequency. In Appendix A, we derive expressions for the the average velocity as a function of the applied field $\mathbf{B}(T)$.

2.4 Topotaxis on an Inclined Surface

We now consider the dynamics of a ferromagnetic roller on an inclined surface subject to a time-periodic magnetic field. To apply the results of the previous section, we make use of three coordinate systems: (1) the *surface* coordinate, (2) the *world* coordinate, and (3) the *particle* coordinate (Fig. 2). The solid plane is located at $z = 0$ in the surface coordinate; the gravity vector is $\mathbf{g}' = [0, 0, -g]^T$ in the world coordinate. The magnetic field vector $\mathbf{B}'(T)$ in the world coordinate is related to the same vector $\mathbf{B}(T)$ in the surface coordinate as $\mathbf{B}(T) = R_1(\alpha)\mathbf{B}'(T)$, where the matrix $R_1(\alpha)$ describes a coordinate rotation about the x-direction by an angle α (Fig. 2). For small angles ($\alpha \ll 1$), equation (20) for the average velocity can be expanded in powers of α as

$$\begin{aligned} \langle \mathbf{U} \rangle &= \omega(\langle \mathbf{U}_{10} \rangle + \alpha \langle \mathbf{U}_{11} \rangle + O(\alpha^2)) \\ &\quad + \omega^2(\langle \mathbf{U}_{20} \rangle + \alpha \langle \mathbf{U}_{21} \rangle + O(\alpha^2)) + O(\omega^3) \end{aligned} \tag{21}$$

where the components of the velocity are determined by the applied field $\mathbf{B}'(T)$. By carefully selecting the field, one can drive particle motions in a particular direction relative to that of the inclined surface.

3 Results & Discussion

We turn now to the following design problem: what time-periodic magnetic field $\mathbf{B}'(T)$ will drive steady particle motion up (or down) an inclined surface? Importantly, the direction of the incline is not known *a priori*; the same field should drive uphill motions regardless of which direction is up. For multiple particles moving independently in a common field $\mathbf{B}'(T)$, the motion of each particle should be directed by the *local* incline of the surface; the same field should drive different particles in different directions depending on the local surface topography. We address this design problem by two complementary approaches—one model-driven, another data-driven—and discuss their respective merits in light of this and other design challenges posed by colloidal robotics. Common to both approaches is the use of symmetry arguments to prevent undesired motions and constrain the design space of possible fields $\mathbf{B}'(T)$.

3.1 Rotational Symmetry

In the absence of an incline ($\alpha = 0$), there should be zero time-averaged motion. We can enforce this condition by selecting external fields $\mathbf{B}'(T)$ with m-fold rotational symmetry about the z' axis. Specifically, we require that the applied field satisfy the condition

$$R_3(\varphi_m)\mathbf{B}'(T) = \mathbf{B}'(T - \varphi_m) \tag{22}$$

where $R_3(\varphi_m)$ describes a coordinate rotation about the z'-axis by an angle $\varphi_m = 2\pi/m$ for a specified integer $m \geq 3$. This condition implies that the rotation of the field by an angle φ_m is equal to a shift in phase of φ_m.

As a result of this symmetry, contributions to the average velocity at zeroth order in the angle α are zero (Appendix B)

$$\langle \mathbf{U}_{10} \rangle = \langle \mathbf{U}_{20} \rangle = 0 \tag{23}$$

Although intuitive, this result is not guaranteed to apply at higher orders in the frequency ω. It is possible that certain fields with rotational symmetry could drive steady particle motions on level surfaces ($\alpha = 0$) at high frequencies; however, we did not observe such symmetry-breaking motions here.

At first order in α, fields with rotational symmetry can drive motions perpendicular to the gradient direction at first order in the frequency ω; however, motions parallel to the gradient direction do not appear until second order in ω. For the scenario in Figure 2, the leading order contribution to particle motion is

$$\langle \mathbf{U}_{11} \rangle = \langle U_x^{(11)} \rangle \mathbf{e}_x \tag{24}$$

which is perpendicular to the gradient direction (Appendix B). This result is potentially problematic: we would prefer the leading order contribution to describe desired motions up (or down) the gradient. Recognizing this issue, we can use the model to design fields that eliminate such undesired motions.

3.2 Model-driven Design

For the present problem, it is possible to identify time-periodic magnetic fields that (1) prohibit undesired motions perpendicular to the gradient direction, and (2) offer control over the direction and speed of desired motions parallel to the gradient direction. One such field—notable for its simplicity and analytical tractability—is given by

$$\mathbf{B}'(T) = \begin{bmatrix} \cos\chi(T)\sin(mT) \\ \sin\chi(T)\sin(mT) \\ \cos(mT) \end{bmatrix} \tag{25}$$

where $m \geq 3$ is an integer that specifies the order of rotational symmetry, and the angle $\chi(T)$ is given by

$$\chi(T) = T - \frac{b}{m}\cos(mT) + \frac{1}{4m}\left(1 + \sqrt{\lambda}\right)^2 \sin(2mT) \tag{26}$$

where b is a free parameter. This field has a constant magnitude but time-varying orientation. It satisfies the rotational symmetry constraint of equation (22). Moreover, it is designed to eliminate undesired motions perpendicular to the gradient at first and second order in the frequency—that is, $\langle U_x^{(11)} \rangle = \langle U_x^{(21)} \rangle = 0$. While there are many such fields that satisfy these criteria; equation (25) was the simplest we could find that allows for close-form expressions of the particle migration velocity.

For this field, the leading order contribution to the average velocity is parallel to the gradient and given by the analytical expression

$$U_y^{(21)} = \kappa \left(C_0(\lambda) + C_b(\lambda) b^2 - C_m(\lambda) m^2 \right) \tag{27}$$

where $C_0(\lambda)$, $C_b(\lambda)$, and $C_m(\lambda)$ are positive order one constants than depend on λ as

$$\begin{aligned} C_0(\lambda) &= (\lambda - 1) \frac{2\lambda^{5/2} + 5\lambda^2 + 2\lambda^{3/2} + 2\lambda - 4\lambda^{1/2} + 1}{32\lambda^{3/2}} \\ C_b(\lambda) &= (\lambda^{1/2} - 1) \frac{2\lambda^2 + 6\lambda^{3/2} + 8\lambda + 3\lambda^{1/2} + 1}{8\lambda^{3/2}(\lambda^{1/2}+1)^2} \\ C_m(\lambda) &= (\lambda - 1) \frac{3\lambda + 1}{8\lambda^{3/2}} \end{aligned} \tag{28}$$

For our default estimate of $\lambda = 1.87$, these constants are $C_0 = 0.334$, $C_b = 0.136$, and $C_m = 0.281$. Importantly, there is no motion when $\lambda = 1$: differences in the resistance to rotation about axes parallel and perpendicular to the surface are essential to drive steady particle motions on inclined surfaces.

According to equation (27) for the migration velocity, we can select large values of b to drive particle motion uphill or large values of m to drive particle motion downhill. Figure 3 illustrates these two scenarios for dimensionless frequency $\omega = 0.005$ and incline angle $\alpha = 0.2$ radians. During steady migration up the inclined surface, the particle zigzags back and forth in the x direction (m times per cycle) as it wiggles its way along the y direction (Fig. 3b,c). Steady migration down the inclined surface is accomplished using a qualitatively different motion whereby the particle rolls along nearly circular orbits (Fig. 3b). In both examples, the approximate migration velocity of equation (27) agrees well with the steady motions computed numerically (Fig. 3c). More generally, the validity of the perturbation expansion requires that $|\dot{\mathbf{B}}| \ll 1$ such that the field varies slowly relative to the particle relaxation rate. For large m or b, this condition implies that $\omega \ll (m^2 + b^2)^{-1/2} \ll 1$.

In dimensionless units, the uphill migration velocity for $b \gg m$ can be approximated as

$$\langle \mathbf{U} \rangle \approx C_b(\lambda) \kappa \alpha b^2 \omega^2 \mathbf{e}_y \tag{29}$$

To maximize the migration velocity, one should increase the product $b\omega$ as much as possible while maintaining the requirement that $b\omega \ll 1$. Assuming that $b\omega \approx 0.3$, the characteristic migration velocity in *dimensional* units is

$$\langle \mathbf{U} \rangle \approx (0.3)^2 \kappa a C_b \omega_0 \alpha \mathbf{e}_y \approx (4.48 \times 10^{-4}) \frac{m B_0 \alpha}{6\pi\eta a^2} \mathbf{e}_y \tag{30}$$

where the second expression assumes a surface separation of $\delta = 0.01a$. For magnetic Janus spheres ($a = 2$ μm, $m = 2.9 \times 10^{-14}$ A m^2)[36] in water, application of a 10 mT field is predicted to drive propulsion speeds of 2 μm/s per radian of incline.

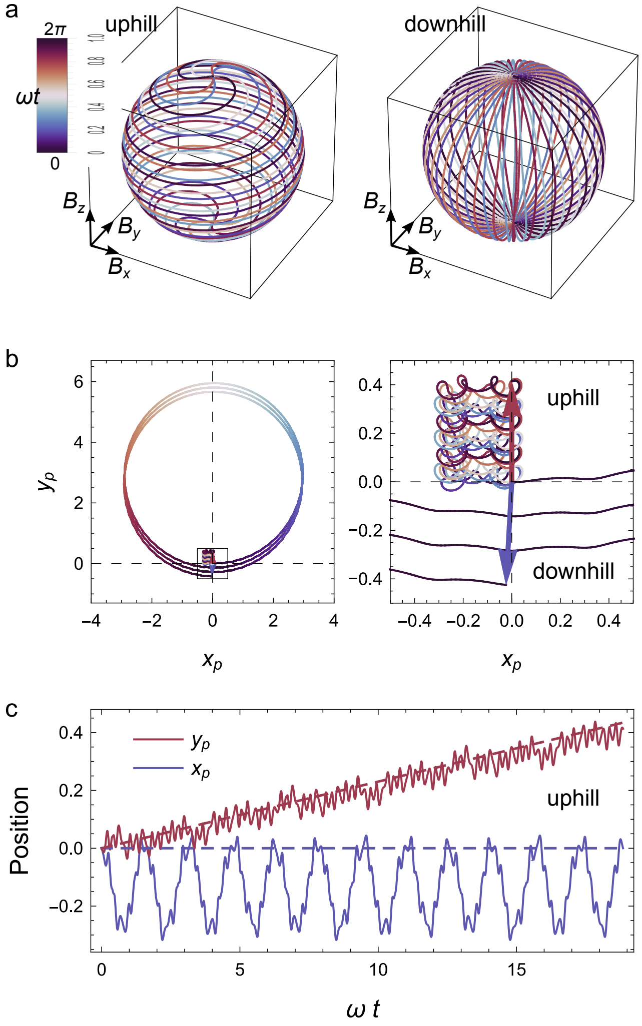

Fig. 3 (a) Two periodic fields $\mathbf{B}'(\omega t)$ from equation (25) designed to drive particle motion uphill (left) and downhill (right). The uphill field has parameters $m = 4$ and $b = 40$; the downhill field has parameters $m = 28$ and $b = 0$. (b) Numerically computed particle trajectories in the xy plane over three oscillation cycles using the fields in (a). The uphill field causes the particle to "wiggle" erratically with an average velocity of $\langle U_y \rangle = 0.022\omega$. The downhill field drives the particle around large circular orbits with a net velocity $\langle U_y \rangle = -0.023\omega$. Here, the dimensionless frequency is $\omega = 0.005$; the incline angle is $\alpha = 0.2$ rad; the hydrodynamic parameters are $\lambda = 1.87$ and $\kappa = 0.108$. (c) Particle dynamics computed numerically (solid curves) compared favorably with the time-averaged dynamics (dashed lines) predicted by equation (27). Data correspond to the uphill trajectory in (b).

Given the result of equation (30), we can now evaluate the validity of our assumption that particle motions due to gravity are negligible. Particle sedimentation down an inclined substrate proceeds with a speed $U_g = \alpha F_g Y_C / [6\pi\eta a (Y_A Y_C - Y_B^2)]$, where F_g is the force of gravity. Comparing with the migration speed in equation (30), this contribution to particle motion is negligible when $F_g \ll 0.014\ m B_0 / a$ assuming a surface separation of $\delta = 0.01a$. Use the above estimates for the moment, radius, and field, this condition implies that the density contrast between the particle and the fluid must be less than $\Delta\rho \ll 6000$ kg/m^3, which is easily achieved in practice for all but the densest particle materials.

In addition to sedimentation, gravitational forces also influence the orientational dynamics of the particle; however, these effects are also negligible when $F_g \ll 0.014\ mB_0/a$ (see Supplementary Information).

3.3 Data-driven Design

The model-driven solution outlined in the previous section represents only one of many possible designs for encoding the autonomous navigation of smooth topographic gradients. By expanding the space of possible designs, it may be possible to discover more effective strategies for topotaxis. Moreover, by using numerical simulations or—in principle—automated experiments, one can explore a wider range of conditions (e.g., higher frequencies) than those allowed by analytical approximations. Most importantly, data-driven design strategies based on the outcomes of simulations or experiments can be used to address design problems for which accurate models are unavailable. In this section, we demonstrate a data-driven approach to design driving fields that encode the rapid migration of ferromagnetic rollers up or down an inclined substrate.

We consider periodic fields $\mathbf{B}(t)$ with a fundamental frequency ω and N harmonics

$$\mathbf{B}'(t) = \sum_{n=0}^{N} \mathbf{b}_n' e^{in\omega t} \tag{31}$$

where $\mathbf{b}_n'$ are constant vectors. Only the real part of the Fourier series is physically meaningful; the prime symbols remind us that the field is specified in the world coordinates. This $6N+3$ dimensional design space is constrained by equation (22), which ensures that the field has m-fold rotational symmetry about the z'-axis. For $n=0$, this constraint implies that $\mathbf{b}_0' = c_0 \mathbf{e}_z'$ where c_0 is a real constant. The first harmonic has Fourier coefficients of the form

$$\mathbf{b}_1' = c_1 \begin{bmatrix} 1 \\ -i \\ 0 \end{bmatrix} + d_1 \begin{bmatrix} i \\ 1 \\ 0 \end{bmatrix} \tag{32}$$

where c_1 and d_1 are real constants that specify the magnitude and phase of a rotating field in the $x'y'$ plane. More generally, there exist rotationally symmetric contributions to the field for $n = 0, 1, km-1, km, km+1$ where k is a positive integer. For higher harmonics equal to a integer multiple of the symmetry order m, the Fourier coefficients have the form

$$\mathbf{b}_n' = c_n \begin{bmatrix} 0 \\ 0 \\ 1 \end{bmatrix} + d_n \begin{bmatrix} 0 \\ 0 \\ i \end{bmatrix} \quad \text{for} \quad n = km \tag{33}$$

Neighboring harmonics with $n = km \pm 1$ have Fourier coefficients of the form

$$\mathbf{b}_n' = c_n \begin{bmatrix} 1 \\ \mp i \\ 0 \end{bmatrix} + d_n \begin{bmatrix} \pm i \\ 1 \\ 0 \end{bmatrix} \quad \text{for} \quad n = km \pm 1 \tag{34}$$

To limit the size of our design space, we fix the number of higher harmonics to $N = m+1$. In this way, the full $6N+3$ dimensional design space is reduced to nine dimensions (namely, c_0, c_1, d_1 c_{m-1}, d_{m-1} c_m, d_m, c_{m+1}, and d_{m+1}). As the phase of the driving field is not important, we set $d_1 = 0$ without loss of generality. Moreover, we found that the static field contribution c_0 does not contribute significantly to topotatic motions (see Supplementary Information); we therefore set $c_0 = 0$. Each of the seven remaining parameters is bounded on the range $[-1, 1]$ to constrain the magnitude of the field.

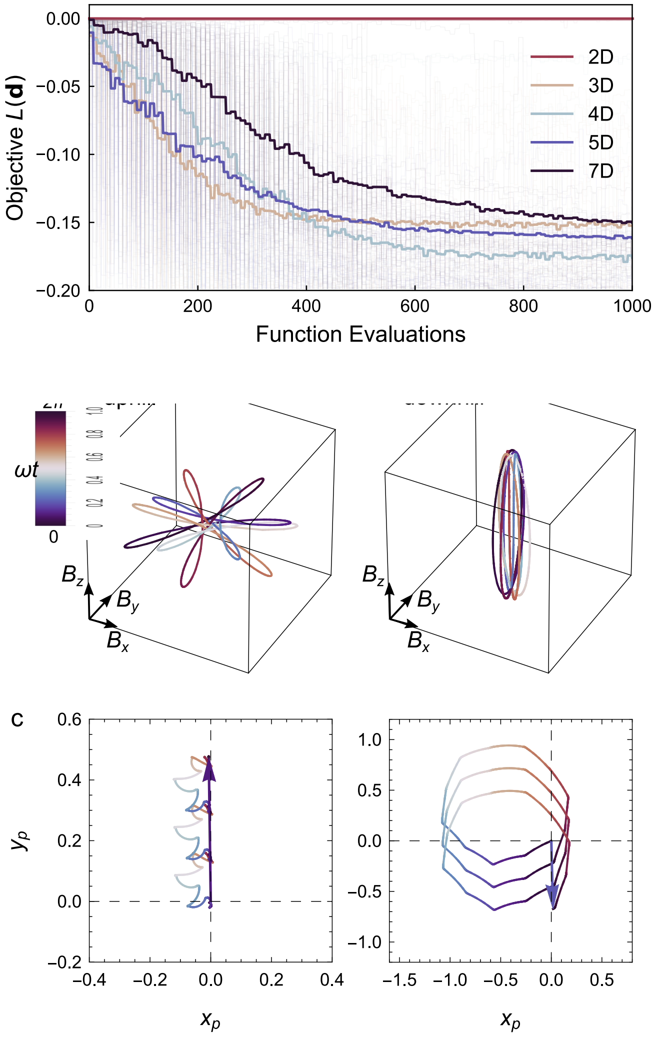

Fig. 4 (a) Convergence plot showing the decrease in the objective function $L(\mathbf{d})$ with increasing function evaluations during optimization via CMA-ES. Different colors correspond to design spaces with different numbers of dimensions. For each design space, optimization is initialized from 50 randomly selected designs (light curves); bold curves show the average performance. (b) Two periodic fields $\mathbf{B}'(\omega t)$ identified by the data-driven process to drive particle motion uphill (left) and downhill (right). The uphill field is characterized by design parameters $c_1 = 0.135$, $c_5 = -0.865$, $d_5 = -0.003$ $c_6 = -0.222$, $d_6 = -0.161$, $c_7 = -0.210$, and $d_7 = -0.771$; the downhill by $c_1 = 0.044$, $c_5 = -0.119$, $d_5 = -0.023$ $c_6 = -0.988$, $d_6 = 0.608$, $c_7 = 0.007$ and $d_7 = -0.089$. (c) Numerically computed particle trajectories in the xy plane over three oscillation cycles using the fields in (b). The drift velocities are $\langle U_y \rangle = 0.0252\omega$ and $\langle U_y \rangle = -0.0357\omega$ for uphill and downhill motion, respectively. In all plots, the symmetry order is $m = 6$; the dimensionless frequency is $\omega = 0.025$; the incline angle is $\alpha = 0.2$ rad; the hydrodynamic parameters are $\lambda = 1.87$ and $\kappa = 0.108$.

Within this design space, we seek fields that minimize the following objective function

$$L(\mathbf{d}) = -\frac{\Delta_y}{1+(10\Delta_x/\Delta_y)^2} \tag{35}$$

where $\mathbf{d}$ is the design vector containing the value of the seven field parameters, and $\mathbf{\Delta}$ is the particle displacement during one oscillation cycle at the periodic steady-state. Minimizing this function favors rapid particle motion up the inclined surface in the positive y direction (Fig. 2); the factor of 10 sets the relative importance between the magnitude and direction of the displacement $\mathbf{\Delta}$. We want the particle to move parallel to the gradient direction (i.e., minimize Δ_x/Δ_y) and to do so as quickly as possible (i.e., maximize Δ_y); the function (35) provides a quantitative formulation of these subjective performance goals. Here, the displacement $\mathbf{\Delta}$ is computed numerically by integrating equations (12)–(15) in time for a specified field. In principle, this information could be obtained from an automated experiment without reference to a physical model. We refer to the resulting designs as *data-driven* as they are guided by observable outcomes of experiments and/or simulations. Here, we specify the rotational order $m = 6$ and the frequency $\omega = 0.025$; however, these quantities could also be treated as additional design variables.

We use the covariance matrix adaptation evolution strategy (CMA-ES)[13,37] to identify designs $\mathbf{d}$ that minimize the objective function $L(\mathbf{d})$ of equation (35). Figure 4a shows the convergence of $L(\mathbf{d})$ towards a minimum value over the course of 1000 function evaluations with 50 independent replicates. Interestingly, the fields identified by this numerical optimization process are qualitatively different from those of the model-driven designs (cf. Fig. 4b and Fig. 3a). Fields optimized to drive particle motion in the uphill direction oscillate in magnitude with only small contributions in the z-direction (Fig. 4b, left). The resulting drift velocity, however, is similar to that of the model-driven design, suggesting that further enhancements in the speed of particle migration are limited. Fields optimized to drive particle motion in the downhill direction use rolling motions with a rotating orientation—not unlike the model-driven design (cf. Fig. 4b, right and Fig. 3a, right).

One potential advantage of the data-driven approach is its ability to design driving fields in the absence of a guiding model. This approach, however, would require ca. 1000 experiments to optimize performance within a known environment—for example, a slope of known orientation. To accelerate this process, we use principal component analysis (PCA) to reduce the dimensionality of the design space and thereby facilitate the search for driving fields with high performance. Briefly, we sample the full 7-dimensional design space at random to identify more than 1000 "good" designs with $L < -0.01$ (see Supplementary Figure S2). These points are then used to identify linear combinations of design variables that describe most of the variance among the points. Using the first $n = 2,3,4$ or 5 of these principle components, we repeat the optimization procedure described above for the full 7-dimensional space. As illustrated in Figure 4a, the use of low-dimensional design spaces enables the identification of high performing fields ($L < -0.1$) more than twice as quickly as in the original space. These results suggest that only ca. 200 function evaluations—or automated experiments—are required to identify suitable driving fields. This data driven methodology may prove useful in design problems for which accurate models are unavailable—for example, the autonomous navigation of particles on asymmetric, ratchet-like topographies.

3.4 Experimental Validation

To test the performance of the designed fields, we quantified the motion of 34 μm ferromagnetic spheres (Spherotech CFM-300-5) in water above a planar glass substrate (Fig. 5a). The particles have a estimated magnetic moment of $m \approx 2 \times 10^{-11}$ A m^2 as determined by analysis of their frequency-dependent rolling speed in a rotating field[19,36] (see Supplementary Information). Gravitational effects are only negligible for these larger particles when the density difference with the liquid is $\Delta\rho \ll 220$ kg/m^3, which is not satisfied in water. To eliminate these effects, we conduct our experiments on a level substrate and instead tilt the magnetic field by an angle α about the x-axis of the surface coordinate. Field-induced particle motions on this simulated incline are captured by optical video microscopy and quantified by particle tracking algorithms (TrackPy). We focus our proof-of-concept experiments on the model-driven design for uphill topotaxis (Fig. 3), for which the migration velocity $\langle \mathbf{U} \rangle$ is well approximated by equation (29).

Figure 5b shows the field induced motions of a single particle subject to time-varying fields with and without a simulated incline of $\alpha = 20°$. In the presence of the incline, the particle migrates along the "up hill" direction at a constant speed of about 2 μm/s. Control experiments at zero incline show particle migration velocities that are one order of magnitude smaller. To further validate the model predictions, we varied the frequency ω of the applied field and measured the average migration velocity in the x and y directions with and without the simulated incline (Fig. 5c). Along the y-direction parallel to the simulated incline, the migration velocity increased quadratically with the frequency ω as predicted by equation (29). By contrast, in the absence of the simulated incline, there was little motion in the either the x or y directions as expected due to the rotational symmetry of the applied field.

The experiments reveal several factors that can potentially complicate the realization of programmable topotaxis. First, heterogeneity in the magnetic particles—namely, their magnetic moments m and their surface separation δ—can lead to different motions in the same driving field. Magnetic rolling experiments at low frequencies ($\omega \ll \omega_o$) show a broad distribution of rolling speeds, which reflect variations in the surface separation δ among the different particles from $\delta \approx 0.1a$ to $\delta \to 0$ (see Supplementary Information). Particles with smaller separations exhibit stronger rotation-translation coupling (i.e., larger κ) and thereby faster field-driven motions like that of Figure 5c. Additionally, the presence of magnetic field gradients can lead to particle migration towards regions of high field strength at speeds that compete with topotaxis. In our experiments, these effects were mitigated by positioning the particle near the center of the three electromag-

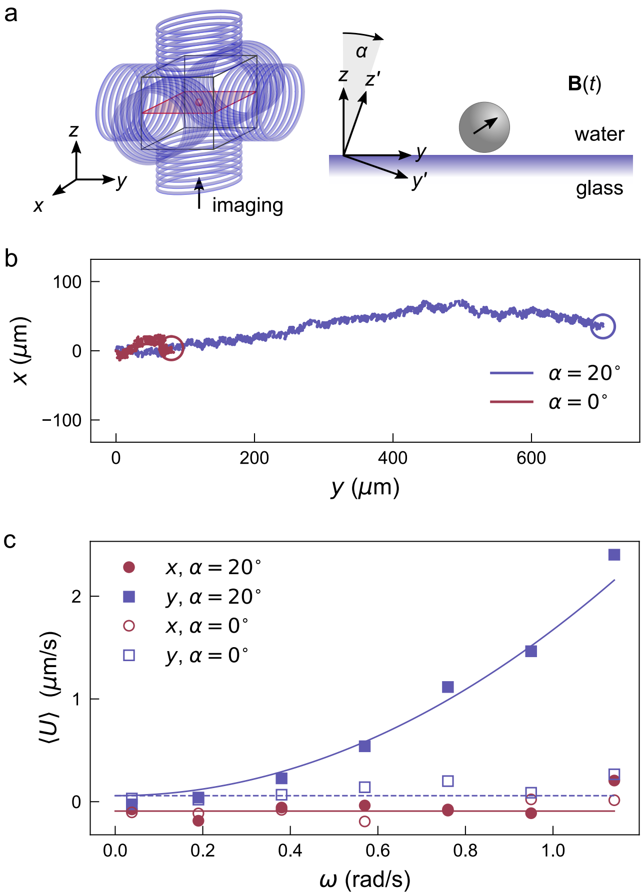

Fig. 5 (a) Schematic illustration of the experimental setup. (b) Reconstructed trajectories for a single particle subject to a time-varying magnetic field with and without a simulated incline of $\alpha = 20^\circ$. The applied field $\mathbf{B}(t)$ corresponds to the model-driven design of equations (25) and (26) with parameters $m = 4$, $b = 40$, and $\lambda = 1.3$ selected for uphill topotaxis (Fig. 3). The field was applied for a duration of five minutes with frequency $\omega = 1.14$ rad/s and field strength $B_0 = 3.0$ mT. (c) Drift velocity $\langle U \rangle$ parallel (y-direction, violet squares) and perpendicular (x-direction, burgundy circles) to the gradient direction as a function of frequency ω for a simulated incline of $\alpha = 20^\circ$ (filled markers) and $\alpha = 0$ (open markers). The curves correspond to best fits of the predicted forms: $\langle U_y \rangle = C_1 \omega^2 \alpha + C_2$ and $\langle U_x \rangle = C_3$ with $C_1 = 4.63$ μm s rad^{-3}, $C_2 = 0.058$ μm/s, $C_3 = -0.091$ μm/s.

nets. One should also consider the frequency-dependent response of the electromagnetic coils to ensure that the applied field is representative of the intended field. Here, the electromagnets have a characteristic response time of $\sim$100 s^{-1}, above which the field is attenuated and shifted in phase. Our experiments use frequency components as fast as $b\omega = 46$ rad/s, at which such effects are present but small. Finally, we emphasize that the current results apply only to individual particles; magnetic and/or hydrodynamic interactions among nearby particles are expected to influence their motion in the driving field. The ability to design fields to direct such collective motions is an interesting target for future work.

4 Conclusions

Programming the autonomous behavior of active or driven colloids requires one to navigate large design spaces in search of those designs with desired performance. In this context, the time-domain of external fields—particularly magnetic fields in 3-dimensions—provide a useful medium for encoding particle behaviors as well as an energy supply for powering them. Here, we applied this general strategy to encode the autonomous navigation of magnetic microspheres on smoothly varying topographic gradients. The simple geometry of the problem allowed us to investigate and compare two strategies for designing the driving field.

Model-driven designs require a detailed understanding of the relationship between the driving field and the resulting particle motions. When available, this understanding can be leveraged to create robust designs under appropriate conditions (e.g., at low frequencies $\omega \ll \omega_o$). Though idealized, these models provide useful insights that guide the design process. For example, one should increase the driving frequency ω as large as possible to maximize desired particle motions that scale as ω^2 relative to undesired motions that scale as ω. At the same time, the driving field must vary slowly enough for the particle's magnetic moment to follow the field without "slipping".

Guided by these and other heuristics, data-driven designs use simulations or automated experiments to probe the quantitative relationship between design and performance that idealized models may fail to capture. In the present context, we found that high performing designs could be identified using ca. 200 simulation outcomes. A series of automated experiments that rely on computer-controlled fields, imaging, and data analysis could conceivably collect as much data within ca. 10 hr assuming 3 min for each experiment. Importantly, such brute-force, evolutionary strategies are capable of discovering useful designs without a model—or any understanding for that matter. We are currently working to extend our experimental platform to further test the theoretical predictions of the present work and to demonstrate data-driven designs for navigating complex structured environments. As in other domains, evolutionary design processes[38,39] are expected to play an important role in programming the autonomous behaviors of colloidal robots.

Conflicts of interest

There are no conflicts to declare.

Acknowledgements

This work was supported by the Center for Bio-Inspired Energy Science, an Energy Frontier Research Center funded by the US Department of Energy, Office of Science, Basic Energy Sciences under Award No. DESC0000989.

Appendix A: Perturbation Solution

We write the governing equations (12) and (13) for the Euler angles $\theta(t)$ and $\psi(t)$ as

$$d_t\theta = \partial_\tau\theta + \omega\partial_T = f(\theta,\psi) \tag{36}$$

$$d_t\psi = \partial_\tau\psi + \omega\partial_T\psi = g(\theta,\psi) \tag{37}$$

Substituting the expansions (16) and (17), we collect like powers in ω and solve the hierarchy of perturbation equations to derive the components of the particle velocity (20) presented in the main text.

Zeroth Order, $O(\omega^0)$

The zeroth order equations are

$$\partial_\tau\theta_0 = f(\theta_0,\psi_0) \tag{38}$$

$$\partial_\tau\psi_0 = g(\theta_0,\psi_0) \tag{39}$$

On time scales of order unity, the time derivatives relax to zero, and the orientation of the particle is specified by the applied field. The resulting solution is

$$\theta_0(\infty,T) = \mathrm{atan2}((B_x^2+B_y^2)^{1/2}, B_z) \tag{40}$$

$$\psi_0(\infty,T) = \mathrm{atan2}(B_x, -B_y) \tag{41}$$

where $\mathrm{atan2}(y,x)$ is the 2-argument arctangent function. Note that the components of the applied field depend on the slow time—for example, $B_x = B_x(T)$.

First Order, $O(\omega^1)$

The first order equations are

$$\partial_T\theta_0 + \partial_\tau\theta_1 = \theta_1\partial_\theta f(\theta_0,\psi_0) + \psi_1\partial_\psi f(\theta_0,\psi_0) \tag{42}$$

$$\partial_T\psi_0 + \partial_\tau\psi_1 = \theta_1\partial_\theta g(\theta_0,\psi_0) + \psi_1\partial_\psi g(\theta_0,\psi_0) \tag{43}$$

Substituting the zeroth order solution (40) and (41), we find the following solution for the first order quantities as $\tau\to\infty$

$$\theta_1(\infty,T) = \frac{B_{xy}\dot{B}_z - (B_x\dot{B}_x + B_y\dot{B}_y)B_z}{B_{xy}B^3} \tag{44}$$

$$\psi_1(\infty,T) = \frac{B(B_y\dot{B}_x - B_x\dot{B}_y)}{B_{xy}^2(\lambda B_{xy}^2 + B_z^2)} \tag{45}$$

where $B = (B_x^2+B_y^2+B_z^2)^{1/2}$ is the field magnitude, $B_{xy} = (B_x^2 + B_y^2)^{1/2}$ is the magnitude of the field projected onto the xy plane, and the dots denote derivatives with respect to the slow time. Using these expressions, the first order contribution to the particle velocity in the x direction is

$$U_x^{(1)}(T) = \kappa\left(\frac{(B_z\dot{B}_x - B_x\dot{B}_z)}{B^2} + (\lambda-1)\frac{B_yB_z(B_x\dot{B}_y - B_y\dot{B}_x)}{B^2(\lambda B_{xy}^2+B_z^2)}\right) \tag{46}$$

The velocity in the y direction can be obtained by permuting the x and y indices.

Second Order, $O(\omega^2)$

The second order equations are

$$\partial_T\theta_1 + \partial_\tau\theta_2 = -B\theta_2 - \frac{B_zB_{xy}}{2B}\psi_1^2 \tag{47}$$

$$\partial_T\psi_1 + \partial_\tau\psi_2 = -\frac{\lambda B_{xy}^2 + B_z^2}{B}\psi_2 - \frac{B_z(B^2-(\lambda-1)B_{xy}^2)}{B_{xy}B}\theta_1\psi_1 \tag{48}$$

In the limit as $\tau\to\infty$, the second order solutions can be expressed in terms of the first order solutions (44) and (45) as

$$\theta_2(\infty,T) = -\frac{1}{B}\partial_T\theta_1 - \frac{B_zB_{xy}}{2B^2}\psi_1^2 \tag{49}$$

$$\psi_2(\infty,T) = -\frac{B}{\lambda B_{xy}^2+B_z^2}\partial_T\psi_1 - \frac{B_z(B^2-(\lambda-1)B_{xy}^2)}{B_{xy}(\lambda B_{xy}^2+B_z^2)}\theta_1\psi_1 \tag{50}$$

The second order contribution to the particle velocity in the x direction is

$$U_x^{(2)}(T) = \kappa\left(\frac{B_yB_z}{B}\psi_2 - \frac{BB_x}{B_{xy}}\theta_2 + \frac{B_xB_z}{2B}\psi_1^2 + \frac{B_yB_z^2}{BB_{xy}}\theta_1\psi_1\right) \tag{51}$$

where θ_2 and ψ_2 are given by equations (49) and (50), θ_1 and ψ_1 by equations (44) and (45). The velocity in the y direction can be obtained by permuting the x and y indices.

Appendix B: Rotational Symmetry

Zeroth Order, $O(\alpha^0)$

For fields $\mathbf{B}'(T)$ with rotational symmetry satisfying equation (22), the average velocity $\langle\mathbf{U}_{10}\rangle$ is identically zero as stated in equation (23). To show this, we first note that an integral over one period of a periodic function is invariant to a shift in phase

$$\langle\mathbf{U}_{10}\rangle = \frac{1}{2\pi}\int_0^{2\pi}\mathbf{U}_{10}(\mathbf{B}'(T-\varphi_m))dT \tag{52}$$

where $\varphi_m = 2\pi/m$. Using equation (22) for rotational symmetry, we can write the average velocity as

$$\langle\mathbf{U}_{10}\rangle = \frac{1}{2\pi}\int_0^{2\pi}\mathbf{U}_{10}(R_3(\varphi_m)\mathbf{B}'(T))dT \tag{53}$$

Similar equations hold for other integer multiples of the angle φ_m. By averaging over the first m multiples, we can write

$$\langle\mathbf{U}_{10}\rangle = \frac{1}{2\pi}\int_0^{2\pi}\left[\frac{1}{m}\sum_{n=0}^{m-1}\mathbf{U}_{10}(R_z(n\varphi_m)\mathbf{B}'(T))\right]dT = 0 \tag{54}$$

where the integrand is identically zero. Note that the instantaneous velocity $\mathbf{U}_{10}$ is given by equation (46) since $\mathbf{B}'(T) = \mathbf{B}(T)$ at zeroth order in α. Using the same arguments, it can be show that the average velocity $\langle\mathbf{U}_{20}\rangle$ is also zero as stated in equation (23).

First Order, $O(\alpha^1)$

For fields $\mathbf{B}'(T)$ with rotational symmetry satisfying equation (22), the average velocity $\langle U_y^{(11)}\rangle$ parallel to the gradient direction is identically zero as implied by equation (24). To show this, we use the rotational symmetry of the field to simplify the integrand as in equation (54) above

$$\langle U_y^{(11)} \rangle = \frac{1}{2\pi}\int_0^{2\pi} \left[\frac{1}{m}\sum_{n=0}^{m-1} U_y^{(10)}(R_z(n\varphi_m)\mathbf{B}'(T)) \right] dT \tag{55}$$

The resulting integral can then be simplified as

$$\langle U_y^{(11)} \rangle = \frac{\kappa}{8\pi}\int_0^{2\pi} \frac{d}{dT} \ln\left(\frac{2(\lambda-1){B'_{xy}}^2}{B'^2} + 2 \right) dT = 0 \tag{56}$$

where the second equality follows from the periodicity of the field. By contrast, the average velocity in the x-direction (perpendicular to the gradient) is non-zero

$$\langle U_x^{(11)} \rangle = \kappa \int_0^{2\pi} \frac{(\lambda(\lambda+1){B'_{xy}}^2 + (3\lambda-1){B'_z}^2)(B'_x \dot{B}'_y - B'_y \dot{B}'_x)}{4\pi(\lambda {B'_{xy}}^2 + {B'_z}^2)^2} dT \tag{57}$$

where the integrand has been simplified using the rotational symmetry of the field.

Notes and references

1 S. Palagi and P. Fischer, *Nat. Rev. Mater.*, 2018, **3**, 113.

2 K. Han, C. W. Shields IV and O. D. Velev, *Adv. Func. Mater.*, 2018, **28**, 1705953.

3 Y. Hong, N. M. Blackman, N. D. Kopp, A. Sen and D. Velegol, *Phys. Rev. Lett.*, 2007, **99**, 178103.

4 T. R. Kline, W. F. Paxton, T. E. Mallouk and A. Sen, *Angew. Chem. Int. Ed.*, 2005, **44**, 744–746.

5 B. Dai, J. Wang, Z. Xiong, X. Zhan, W. Dai, C.-C. Li, S.-P. Feng and J. Tang, *Nat. Nanotechnol.*, 2016, **11**, 1087.

6 C. Lozano, B. Ten Hagen, H. Löwen and C. Bechinger, *Nat. Commun..*, 2016, **7**, 12828.

7 J. Palacci, S. Sacanna, A. Abramian, J. Barral, K. Hanson, A. Y. Grosberg, D. J. Pine and P. M. Chaikin, *Sci. Adv.*, 2015, **1**, e1400214.

8 L. Ren, D. Zhou, Z. Mao, P. Xu, T. J. Huang and T. E. Mallouk, *ACS Nano*, 2017, **11**, 10591–10598.

9 B. Liebchen, P. Monderkamp, B. ten Hagen and H. Löwen, *Phys. Rev. Lett.*, 2018, **120**, 208002.

10 A. I. Campbell and S. J. Ebbens, *Langmuir*, 2013, **29**, 14066–14073.

11 B. Ten Hagen, F. Kümmel, R. Wittkowski, D. Takagi, H. Löwen and C. Bechinger, *Nat. Commun.*, 2014, **5**, 4829.

12 L. Alvarez, M. Fernandez-Rodriguez, A. Alegria, S. Arrese-Igor, K. Zhao, M. Kröger and L. Isa, *arXiv preprint arXiv:2009.08382*, 2020.

13 Y. Dou and K. J. Bishop, *Phys. Rev. Res.*, 2019, **1**, 032030.

14 A. M. Brooks, S. Sabrina and K. J. M. Bishop, *Proc. Natl. Acad. Sci. USA*, 2018, **115**, E1090–E1099.

15 Y. Alapan, B. Yigit, O. Beker, A. F. Demirörs and M. Sitti, *Nat. Mater.*, 2019, 1.

16 J. G. Lee, A. M. Brooks, W. A. Shelton, K. J. M. Bishop and B. Bharti, *Nat. Commun.*, 2019, **10**, 2575.

17 X. J. Janssen, A. J. Schellekens, K. van Ommering, L. J. van IJzendoorn and M. W. Prins, *Biosens. Bioelectron.*, 2009, **24**, 1937–1941.

18 J. W. Swan and J. F. Brady, *Phys. Fluids*, 2007, **19**, 113306.

19 M. Driscoll, B. Delmotte, M. Youssef, S. Sacanna, A. Donev and P. Chaikin, *Nat. Phys.*, 2017, **13**, 375–380.

20 P. Tierno, R. Golestanian, I. Pagonabarraga and F. Sagués, *Phys. Rev. Lett.*, 2008, **101**, 218304.

21 J. Yan, S. C. Bae and S. Granick, *Soft Matter*, 2015, **11**, 147–153.

22 A. Kaiser, A. Snezhko and I. S. Aranson, *Sci. Adv.*, 2017, **3**, e1601469.

23 H. Xie, M. Sun, X. Fan, Z. Lin, W. Chen, L. Wang, L. Dong and Q. He, *Sci. Robot.*, 2019, **4**, eaav8006.

24 B. Yigit, Y. Alapan and M. Sitti, *Adv. Sci.*, 2019, **6**, 1801837.

25 F. Martinez-Pedrero, A. Ortiz-Ambriz, I. Pagonabarraga and P. Tierno, *Phys. Rev. Lett.*, 2015, **115**, 138301.

26 T. O. Tasci, P. S. Herson, K. B. Neeves and D. W. Marr, *Nat. Commun.*, 2016, **7**, 10225.

27 L. Zhang, T. Petit, Y. Lu, B. E. Kratochvil, K. E. Peyer, R. Pei, J. Lou and B. J. Nelson, *ACS Nano*, 2010, **4**, 6228–6234.

28 T. Yang, A. Tomaka, T. O. Tasci, K. B. Neeves, N. Wu and D. W. Marr, *Sci. Robot.*, 2019, **4**, eaaw9525.

29 J. S. Park, D. H. Kim and A. Levchenko, *Biophys. J.*, 2018, **114**, 1257–1263.

30 M. E. O'neill, *Mathematika*, 1964, **11**, 67–74.

31 W. W. Dean and M. M. O'Neill, *Mathematika*, 1963, **10**, 13–24.

32 H. Brenner, *Chem. Eng. Sci.*, 1961, **16**, 242–251.

33 G. B. Jeffrey, *Proc. London Math. Soc.*, 1915, **14**, 327–338.

34 J. Diebel, *Matrix*, 2006, **58**, 1–35.

35 S. H. Strogatz, *Nonlinear Dynamics And Chaos*, Westview Press, 2nd edn, 2015.

36 W. Fei, M. M. Driscoll, P. M. Chaikin and K. J. Bishop, *Soft Matter*, 2018, **14**, 4661–4665.

37 N. Hansen, S. D. Müller and P. Koumoutsakos, *Evol. Comput.*, 2003, **11**, 1–18.

38 H. Lipson, *Biomimetics*, 2005, **17**, 129–155.

39 J. Hiller and H. Lipson, *IEEE Trans. Robot.*, 2011, **28**, 457–466.

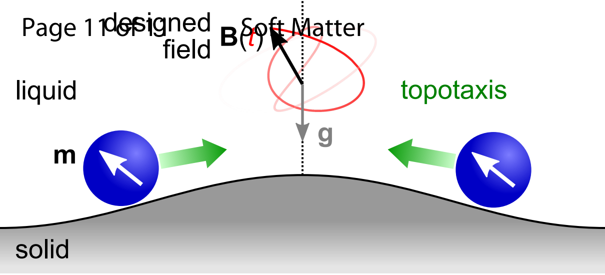
designed field
$\mathbf{B}(t)$
liquid
topotaxis
g
m
solid